

# SCIENTIFIC REPORTS



OPEN

## Novel Two-Dimensional Mechano-Electric Generators and Sensors Based on Transition Metal Dichalcogenides

Sheng Yu, Kwesi Eshun, Hao Zhu & Qiliang Li

Received: 07 April 2015

Accepted: 13 July 2015

Published: 04 August 2015

Transition metal dichalcogenides (TMDCs), such as  $\text{MoS}_2$  and  $\text{WSe}_2$ , provide two-dimensional atomic crystals with semiconductor band gap. In this work, we present a design of new mechano-electric generators and sensors based on transition metal dichalcogenide nanoribbon PN junctions and heterojunctions. The mechano-electric conversion was simulated by using a first-principle calculation. The output voltage of  $\text{MoS}_2$  nanoribbon PN junction increases with strain, reaching 0.036V at 1% strain and 0.31V at 8% strain, much larger than the reported results. Our study indicates that the length, width and layer number of TMDC nanoribbon PN junctions have an interesting but different impact on the voltage output. Also, the results indicate that doping position and concentration only cause a small fluctuation in the output voltage. These results have been compared with the mechano-electric conversion of TMDC heterojunctions. Such novel mechano-electric generators and sensors are very attractive for applications in future self-powered, wearable electronics and systems.

Mechanical energy is one of the most ubiquitous energy sources in the environments and is readily accessible from the human activities. Therefore, the conversion of mechanical energy into electricity offers an immediate, stand-alone power support for remote control systems, wearable electronics, wireless sensing and remote battery charging<sup>1–6</sup>. Piezoelectric transducer is the most distinguished technique for harvesting vibration based energy by its high power output and relatively low-cost manufacturing<sup>7</sup>. Recently, the piezoelectric properties of nanowires have been widely studied for potential applications in sensors, transducers, energy conversion and electronics<sup>8,9</sup>. The power generators based on piezoelectric nanostructures were successfully designed and fabricated<sup>10–12</sup>. The coupling of semiconductor and piezoelectric properties in one-dimensional (1D) ZnO nanowires (NWs) in a nanogenerator was reported with excellent power conversion efficiency from 17% to 30%<sup>13</sup>. However, the difficulty in aligning 1D ZnO NWs may hinder high-performance applications in Nanoelectromechanical Systems (NEMS)<sup>13–16</sup>.

Two-dimensional (2D) layered materials, such as hexagonal boron nitride (h-BN) and transition metal dichalcogenides (TMDCs)<sup>16–18</sup>, have gained considerable attentions for electronic applications. Their mechanical properties, possible application in body movement, muscle stretching and blood vessel contraction<sup>19,20</sup>, have also been studied. The  $\text{MoS}_2$  monolayer, a typical member of 2D TMDCs, becomes piezoelectric after exfoliation from the bulk crystal whereas the inversion symmetry is broken<sup>21,22</sup>. The asymmetry leads to valley polarization caused by valley-selective circular dichroism. This attracts potential applications in valleytronic devices<sup>23,24</sup>. Therefore,  $\text{MoS}_2$  nanostructures have become promising in NEMS application<sup>25,26</sup> in nanopiezotronics, a rapidly emerging field.

The piezoelectric properties and applications of  $\text{MoS}_2$  monolayers, such as mechanical energy harvesting and piezotronic sensing, have very recently been explored experimentally<sup>25,26</sup>. Angular dependence of inversion symmetry has been measured by optical second-harmonic generation (SHG)<sup>27</sup>, indicating that it is mostly broken along armchair direction while preserves along zigzag direction. The absence

Department of Electrical and Computer Engineering, George Mason University Fairfax, VA 22033 USA.  
Correspondence and requests for materials should be addressed to S.Y. (email: syu12@masonlive.gmu.edu)

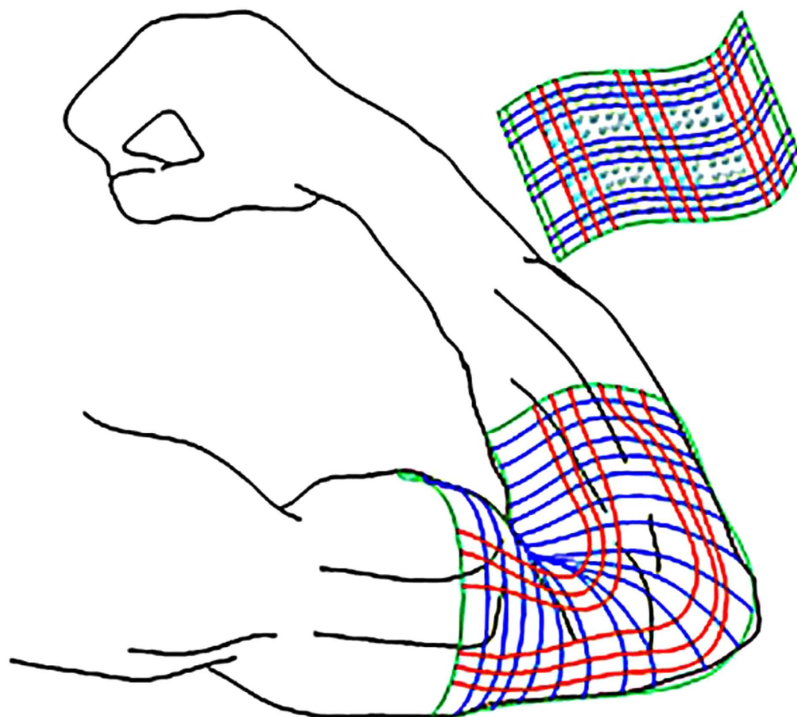


**Figure 1.** Carry-on electronics with mechano-electric generator based on 2D semiconductors.

of centrosymmetry endows MoS<sub>2</sub> monolayer with piezoelectricity along the armchair direction<sup>19</sup>. An open-circuit voltage of 18 mV has been demonstrated at 0.53% strain along the armchair direction<sup>26</sup> in a MoS<sub>2</sub> monolayer of a dimension of 10 μm in length and 5 μm in width. This output voltage is quite small. Enhancement of output performance is very important for further application of 2D materials in mechanical-to-electric generators.

In this work, we report a novel mechano-electric conversion device based on TMDC nanoribbon PN junctions and heterojunctions. As shown in Fig. 1(a), a TMDC nanoribbon mechano-electric generator can be used to convert human muscle stretching power to support wearable electronics. Our first-principle calculation has shown that high output voltages, 0.036 V and 0.31 V at 1% and 8% strain, respectively, can be achieved in a 1.5 nm × 5 nm MoS<sub>2</sub> nanoribbon PN junction. In consideration of the small size of nanoribbon, this mechano-electric generator has a high conversion voltage and its performance can be improved significantly by a series of connection<sup>26</sup>. Our study indicates the mechano-electric conversion of 2D TMDC PN junction is better than that of the heterojunction. This work is the first study of designing 2D TMDC junctions for application in high-performance mechano-electric conversion, suggesting a new way of using 2D TMDCs for future nanogenerators and sensors.

### Methods in Simulation

In this work, the energy diagrams of 2D TMDC nanoribbon PN junctions and heterojunctions have been calculated by first principle calculations carried out by the density functional theory (DFT) in Virtual Nanolab ATK package<sup>28</sup>. The n-type and p-type TMDCs are achieved by substitutional doping. The Localized Density Approximation (LDA) exchange correlation with a Double Zeta Polarized (DZP) basis was used with a mesh cut-off energy of 150 Ry<sup>29</sup>. We used 1 × 1 × 50 Monkhorst-Pack k-grid mesh in this simulation with more k-points in transport direction<sup>30</sup>. All atomic positions and lattice constants were optimized by using the Generalized Gradient Approximations (GGA)<sup>31</sup> with the maximum Hellmann-Feynman forces of 0.05 eV/Å. Pulay-mixer algorithm was employed as iteration control parameter with a strict tolerance value of 10<sup>-5</sup><sup>32</sup>. The maximum number of fully self-consistent field (SCF) iteration steps was set to 1000<sup>29</sup>. The electronic temperature was set to 300 K for all the simulations. The self-consistent field calculations were checked strictly to guarantee fully converging within the iteration steps.

In order to clearly illustrate the design and characteristics of TMDC junction mechano-electric converters, the results are reported as follows: (1) The intrinsic piezoelectricity of 2D infinite MoS<sub>2</sub> monolayer was studied. (2) The PN junction-based device electric output performance was evaluated. (3) Effects of sizes (width, length and layer number) on output voltages were investigated. (4) The fluctuation in output voltage induced by various doping positions and concentrations was studied. (5) The mechano-electric conversion of TMDC nanoribbon heterojunctions were studied and compared with

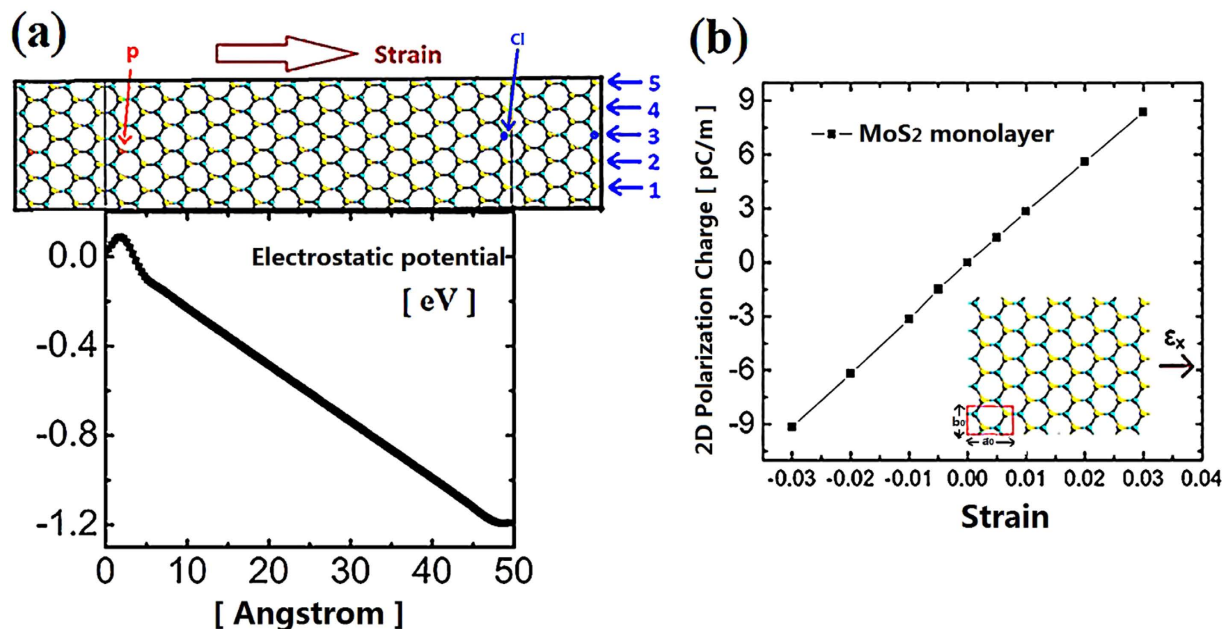


**Figure 2.** (a) Configuration of our designed device, where S atoms are yellow; Mo atoms are cyan; P atom is red and Cl atom is blue. The left and right rectangles represent the left and right electrode. P replaces S at the middle position of left edge of center region. Cl replaces S at the middle position of right edge of center region. (b) The electrostatic potential as a function of position in the central region under zero strain. (c) The polarization charge as the function of strain along in-plane armchair direction

that of PN junctions. Finally, the mechano-electric conversion of various designs based on 2D TMDCs was analyzed and compared.

## Results and Discussion

The basic MoS<sub>2</sub> monolayer PN junction was configured as Fig. 2(a). The model is divided into three regions: left electrode, right electrode, and central region. The central scattering region consists of  $5 \times 9$  unit cells: the width is composed of 5 periodic unit cells in zigzag direction and 9 basic lattice lengths are included in armchair direction, which is designed as transport direction in this study. In the transport direction Dirichlet boundary condition was applied on the two opposite electrodes, in which the electric potential was held homogeneously across the boundary. Neumann condition was employed on the other two directions, in which the electric field was held homogeneously at the boundary. MoS<sub>2</sub> nanoribbon exhibits intrinsic semiconducting property and strongest piezoelectricity along the armchair direction while metallicity and highly crystal inversion symmetry are demonstrated in zigzag direction<sup>33,34</sup>. The coupled semiconducting and piezoelectric properties are responsible for the mechanism of power generator<sup>35</sup>. Substituting sulfur (S) by chlorine (Cl) shifts the Fermi level towards conduction bands, resulting in n-type doping while the inverse p-type doping is realized by the replacement of phosphorus (P). The impurity density on both sides is chosen to be  $10^{13} \text{ cm}^{-2}$  within reasonable computational burden<sup>36</sup>. Fig. 2(b) displays the electrostatic potential as a function of position in the unstrained central region. As shown it is decreasing monotonically along the transport direction and the electrostatic potential dropping (EPD) is 1.174 eV at right edge with respect to the left counterpart. This is consistent with our design that p-type is realized at the left side while the right side is n-type.

### Intrinsic piezoelectricity of 2D MoS<sub>2</sub> monolayer

Firstly, the intrinsic piezoelectricity of MoS<sub>2</sub> monolayer is investigated. Noncentrosymmetric lattice structure is necessary for a material to be piezoelectric<sup>37,38</sup>. The three-dimensional (3D) bulk stacked-layer h-BN and 2H-TMDC crystals are centrosymmetric due to their experimentally observed antiparallel stacking sequence<sup>39</sup>. However, the two dimensional (2D) monolayer of TMDCs, such as MoS<sub>2</sub>, WSe<sub>2</sub>, WS<sub>2</sub>, MoSe<sub>2</sub> etc., which have been successfully fabricated by exfoliation from their 3D bulk materials<sup>40–43</sup>, exhibits noncentrosymmetric crystal structure<sup>22</sup>. This noncentrosymmetry stems from the particular dislocated stacks of the different layers composed by chalcogen atoms and transition elements and accordingly results in the absence of inversion center. As a typical member of TMDCs, 2D MoS<sub>2</sub> monolayer is naturally piezoelectric. Figure 2(c) shows its polarization charge as the function of strain applied along in-plane armchair direction. In this work, the strain is evaluated as the lattice changing percentage. We defined  $\epsilon_x \equiv \Delta a_0 / a_0$ , where  $\Delta a_0$  is the increase of lattice constant  $a_0$  due to the strain.  $a_0 = 5.47 \text{ \AA}$ , signifying the lattice constant along the transport direction (armchair direction). The coefficient  $e11$ ,

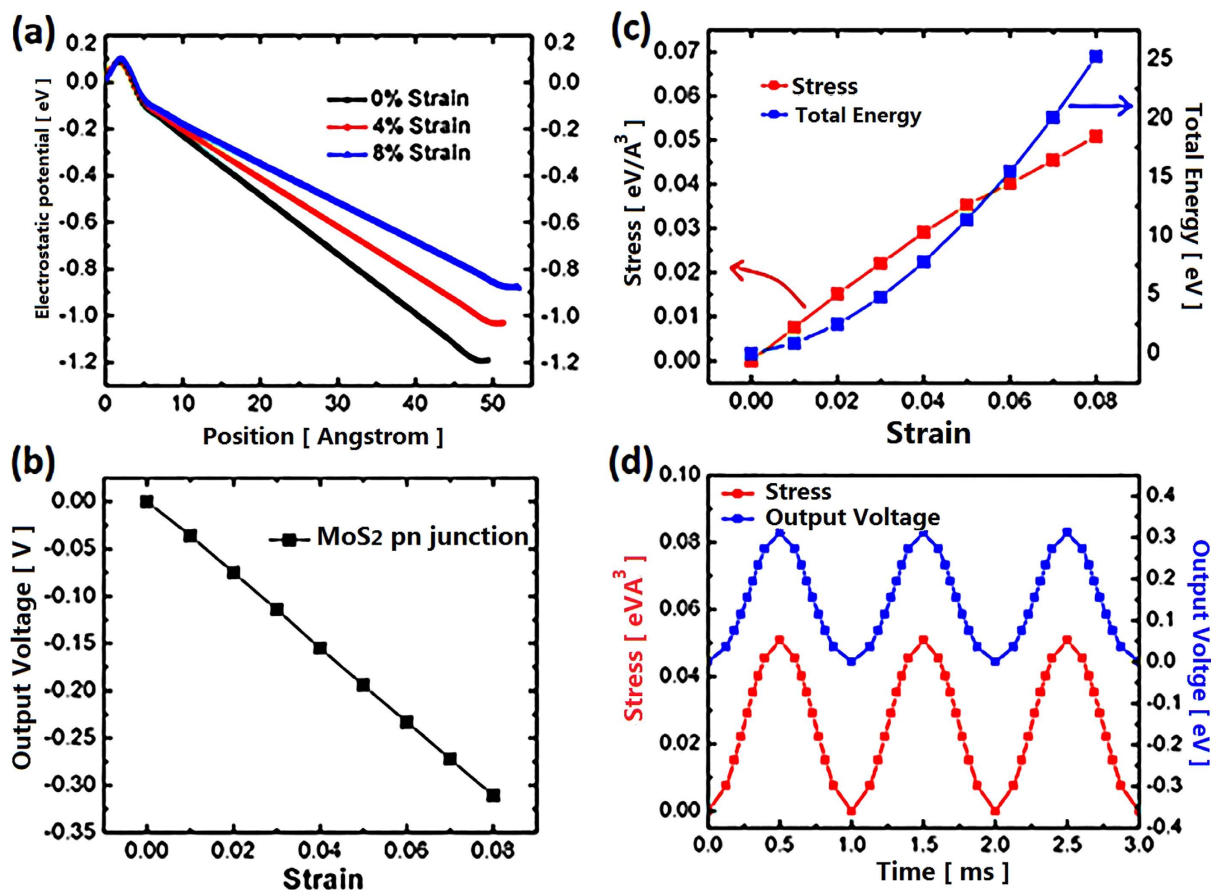


**Figure 3.** (a) 0%, 4% and 8% tensile strain modulated electrostatic potential along transport direction in the central region. (b) The output voltage as a function of strain. The negative value in our study denotes the electrical potential in left electrode is higher than right electrode. (c) The stress and total energy of the central region of our model as a function of strain. (d) Red: stress in sine waveform-time domain is laterally applied on our device. Blue: the output voltage response.

defined as the slope of linear fit line for charge vs. strain curve, reveals the change in polarization along armchair direction per area by strain<sup>19</sup>. Our estimation of  $\epsilon_{11}$  is  $2.98 \times 10^{-10}$  C/m, which is very close to the experimentally reported  $2.90 \times 10^{-10}$  C/m<sup>25</sup>.

### PN junction MoS<sub>2</sub> nanoribbon based device

Secondly, the electronic property of our model under lateral strain has been simulated. The strain given by  $\epsilon = (L - L_0)/L_0$  is initially applied along transport direction, where  $L_0$  and  $L$  is the equilibrium length along the transport direction of the unstrained and strained device, respectively. Fig. 3(a) reveals the electrostatic potential distribution along the transport direction in the central region for the device applied by 0%, 4% and 8% tensile strain, respectively. The central region was extended from 49.2 Å to 53.2 Å in length by 8% strain. As shown the structure under 8% strain has the smallest EPD. EPD reduces from 1.174 V for unstrained structure to 0.878 V for the structure under 8% strain. Fig. 3(b) demonstrates the output voltage as a function of strain applied along the transport direction. The absolute value of output voltage is linearly increasing by larger strain. The maximum output voltage is 0.310 V in the case of 8% strain. The negative value denotes that the electrical potential at left electrode is higher than that of right electrode and therefore the left side serves as the anode while the right counterpart is the cathode in our device. Our study suggests a nano-generator with excellent performance, which has output of ~20 mV in small size (5 nm × 1.5 nm) under 0.5% strain. This indicates significantly enhanced performance by doping and PN junction based device over undoped MoS<sub>2</sub> nanosheet in large area<sup>26</sup>. This tremendous improvement in output is attributed to the strongly enhanced polarization between bipolar atoms induced by the coupled built-in electric field and external strain.

Next, we investigate the mechanical property of our device based on PN junction. Fig. 3(c) demonstrates the variation of total energy with uniaxial strain applied along transport direction. The total energy ( $E_{\text{total}}$ ) is increasing monotonically as the increasing strain ( $\epsilon$ ). The slope of this curved line given by  $dE_{\text{total}}/d\epsilon$  is also rising by the increasing strain. The evolution of the stress with strain is estimated by

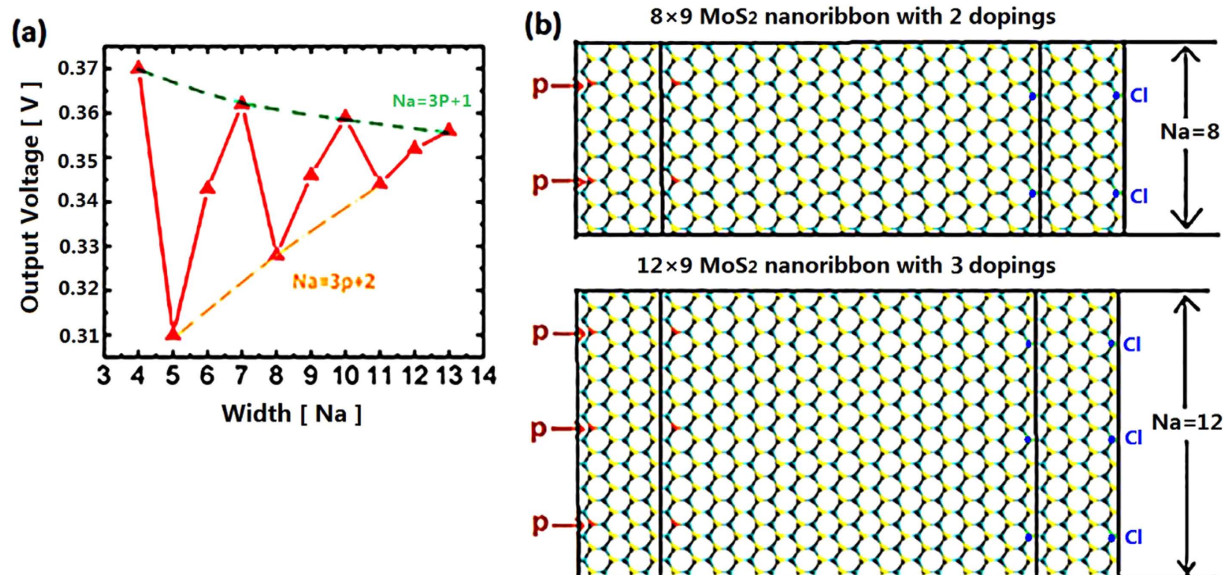


**Figure 4. The investigation on width effect.** (a) The evolution of output voltage with MoS2 nanoribbon width. All the structures are keeping one doping atom at each side. (b) Configuration of nanoribbon with width ( $N_a = 8$ ,  $N_a = 12$ ) by 2 doping and 3 doping atoms, respectively.

the mathematic expression:  $\bar{\sigma} = \frac{1}{V} dE_{\text{total}}/d\varepsilon$ , where  $V$  is the volume of our sampled system<sup>44</sup>. The orthorhombic cube with the total volume of  $9.6 \text{ nm}^3$  was sampled in our study. The stress required for deformation intensity denoted by strain  $\varepsilon$  is increasing monotonically with the larger strain. The stress vs. strain relation keeps good linearity within the small strain range  $0 \leq \varepsilon \leq 3\%$  and the elastic modulus  $C$  is keeping constant by the expression:  $C = d\bar{\sigma}/d\varepsilon$ . Previous report indicated that this parameter can remain constant within small strain ( $-2\% \leq \varepsilon \leq 2\%$ ) for MoS<sub>2</sub> monolayer<sup>45,46</sup>. For the larger strain from 4% up to 8%, this relation slightly deviates from linearity and accordingly the elastic modulus  $C$  reduces. Fig. 3(d) shows the output voltage response for our device under laterally applied stress in Sine waveform-time domain. The periodic time of our dynamic stress is 1ms. Therefore a proper assumption can be suggested that there is negligible delay between input force and output voltage phase<sup>47</sup>. Experimentally, the stress can be realized by bending the substrate periodically<sup>26</sup>. For the mathematic expression of time dependent stress, we deduce it as following:

$$\text{Stress} = \frac{A}{2} \sin[2k\pi(t - 0.25m)] + \frac{A}{2} = A \sin^2(k\pi t) \quad (1)$$

where  $A$  is the maximum stress with the value of  $0.051 \text{ eV}/\text{\AA}^3$ , which induces 8% strain. As shown the maximum output voltage  $\sim 0.310 \text{ V}$  is reached at the maximum stress.

### Effects of Sizes

The evolution of the output voltage with the nanoribbon width ( $N_a$ ) was also investigated. The nanoribbon width is denoted by periodical number of unit cells in zigzag direction vertical to the transport direction. For each structure with incremental width, one doping atom was kept at the center of lateral edge. The length of nanoribbon was kept 9 periodic unit cells in the transport direction. As displayed in Fig. 4(a), the output voltage oscillations are observed for the narrow ribbons, and those nanoribbons of  $N_a = 3p + 1$  (where  $p$  is an integer) have larger output than the neighboring two nanoribbons. With increasing width, the output voltage finally converges to a constant value  $\sim 0.355 \text{ V}$ . The enlarged size will attenuate the doping concentration, and might lead to unexpected impact on the performance of our device. To clarify this issue, two pairs of phosphorus and chlorine doping atoms are introduced in 8-width structure (Fig. 4(b)), and also, three pairs of doping atoms are introduced in 12-width nanoribbon (Fig. 4(c)). The doping concentration of these structures are keeping the same as 4-width structure with one pair of doping atoms. The output voltage for these two structures are  $0.328 \text{ V}$  and  $0.346 \text{ V}$ , indicating slight difference with one doping structure of 8-width ( $0.328 \text{ V}$ ) and 12-width ( $0.352 \text{ V}$ ), respectively. It should be noted that the output of the structure with low doping concentration is slightly higher than that of the highly doping structure. This issue will be discussed in part **doping effect**.

In addition to the width effect, we also investigate the influence of nanoribbon length on the output performance. As displayed by Fig. 5(a) the length of nanoribbon is defined by the periodic lattice number ( $N_b$ ) of the central region in the transport direction (armchair direction). The width number ( $N_a$ ) is kept

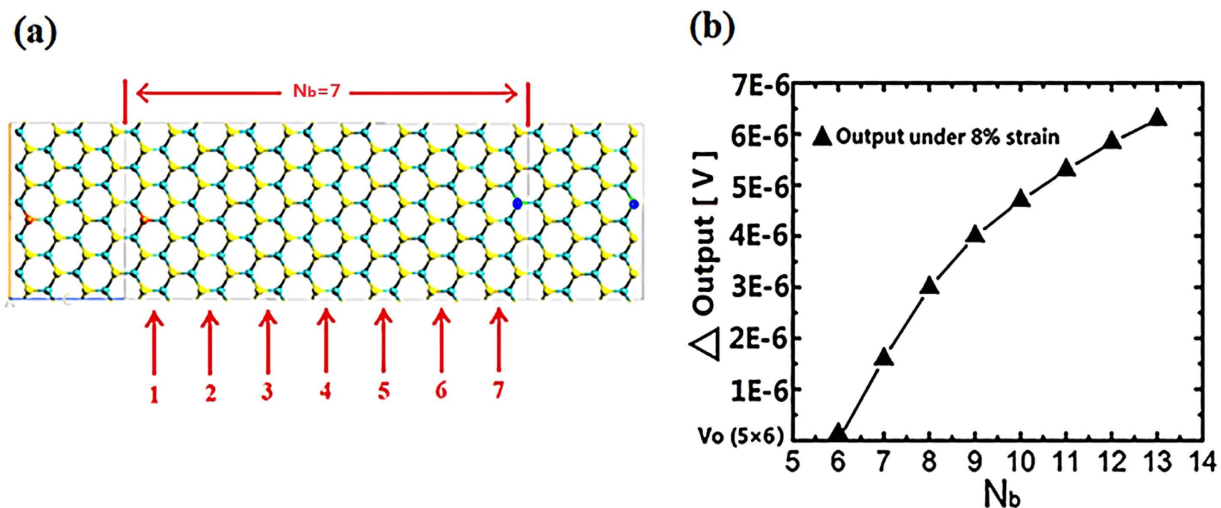


**Figure 5. The investigation on length effect:** (a) Definition of length for MoS<sub>2</sub> nanoribbon. (b) Comparison of the output voltage for structures with different lengths. The output of 5 × 6 is 0.3103446 V, setting as the reference value.

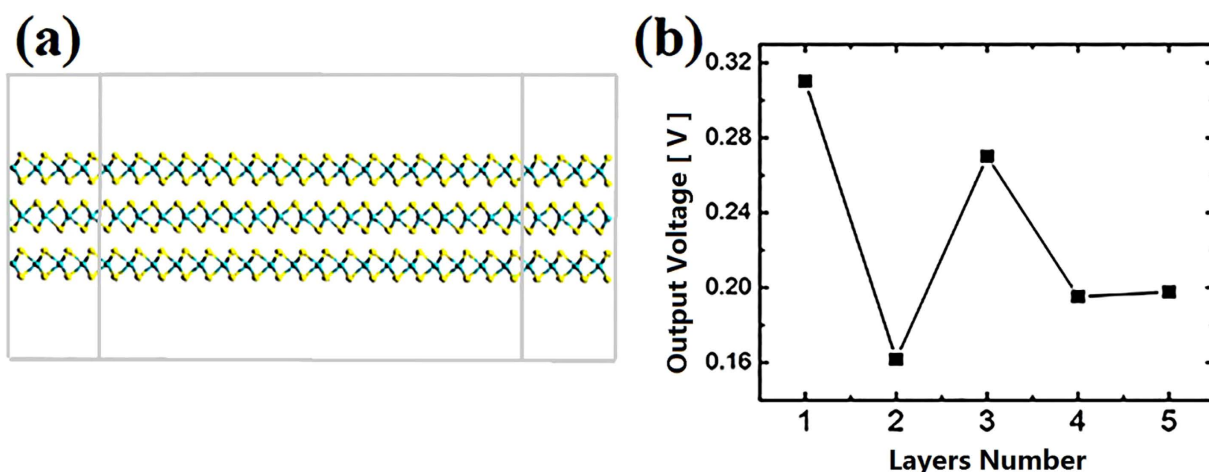


**Figure 6. The investigation on layers effect:** (a) Configuration of 3 layers MoS<sub>2</sub> mechano-electric converter. Each layer is doping by a pair of P and Cl, respectively. (b) Output voltage for device under 8% strain as a function of layer number.

constant value of 5 for all the investigations on length effect. The output voltage for the device under 8% strain as a function of  $N_b$  is shown in Fig. 5(b). The output voltage of the nanoribbon with  $N_b = 6$  is 0.3103446 V, setting as the reference value. The output voltage is slightly increasing by the order of magnitude of  $10^{-6}$  V with increasing  $N_b$ . The rising rate ( $\Delta\text{Output}/\Delta N_b$ ) reduces as larger  $N_b$ , indicating that the output will saturate to a constant value under sufficiently large  $N_b$ . Our study indicates that the structure length has negligible effect on the output voltage.

We also investigated the output voltage as a function of layer number of MoS<sub>2</sub> stacked structure. Fig. 6(a) shows the configuration of 3 layers MoS<sub>2</sub> mechano-electric converter. Each layer is doping by a pair of P and Cl, respectively. P replaces S at left side while Cl is doping at right side. As demonstrated by Fig. 6(b), the output voltage exhibits a fluctuant behavior as increasing layers. It reaches maximum of 0.310 V by single layer, while is reducing significantly to 0.16 V by 2 layers stacked structure. As limited by the simulation complexity and its converging difficulty, we only put forward our investigation to 5 layers. However, a reasonable speculation can be made that the output voltage finally converges to a constant value as increasing layer number, which is trended similarly as that tuned by increasing width. In experiments the output voltage of undoped MoS<sub>2</sub> in large area shows a proportional relation with the second-harmonic generation (SHG) intensity for stacked structures: MoS<sub>2</sub> flakes stacked by odd number of layers exhibited strong piezoelectricity along armchair direction, while the output voltage disappeared

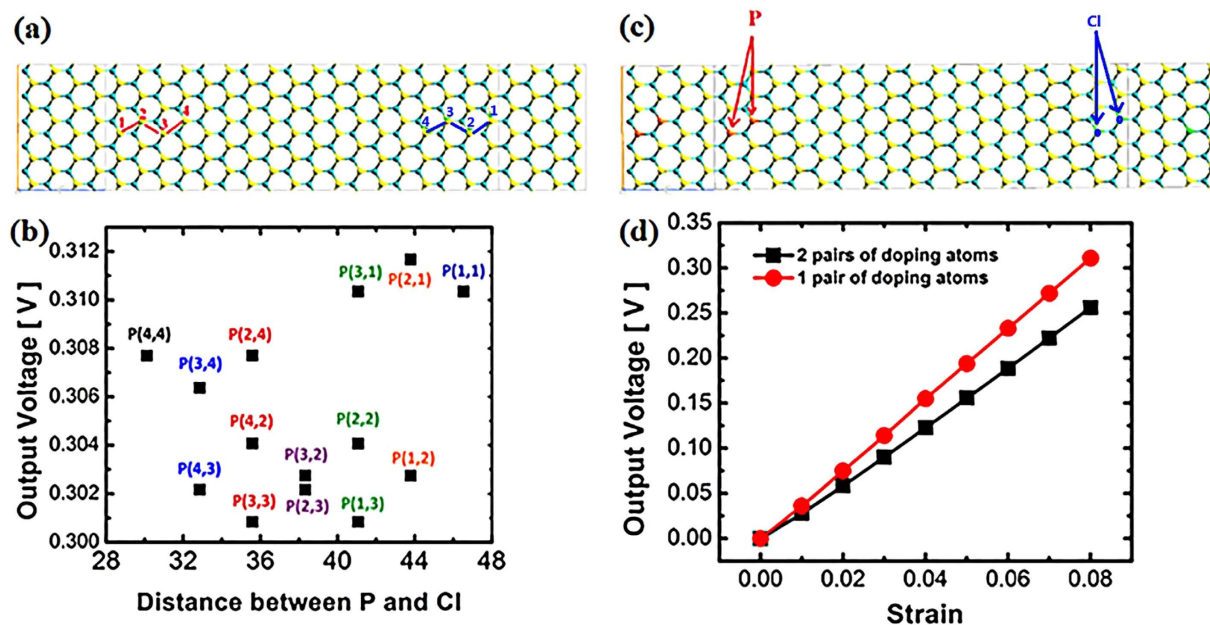


**Figure 7. The investigation on doping effect:** (a) The various combinational doping positions of P and Cl, denoted by P(m, n). As displayed, m, n are the atomic ordinal of P and Cl. (b) The output voltage (under 8% strain) as a function of doping position P(m, n). (c) Configuration of 2 pairs of doping atoms. (d) Comparison of output performance between 2 pairs of doping and 1 pair of doping structure.

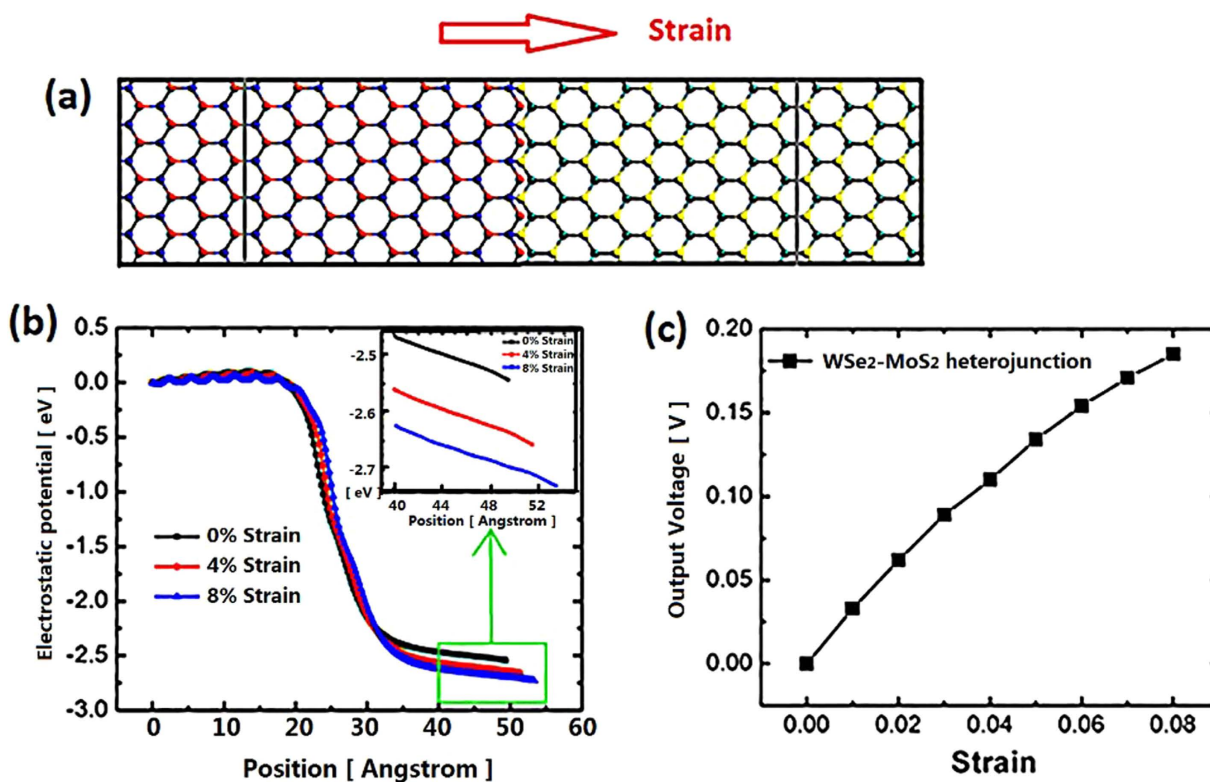


**Figure 8. (a)** Configuration of nano-power generator based on WSe<sub>2</sub> and MoS<sub>2</sub> heterojunction. The left part consists of WSe<sub>2</sub> and the right part is MoS<sub>2</sub>, where Se atoms are blue, W atoms are red, S atoms are yellow and Mo atom are cyan. (b) 0%, 4% and 8% tensile strain modulated electrostatic potential along transport direction in the central region for device displayed in Fig. 5(a). Inset: the enlarged view of electrostatic potential within the region from 40 Å to 55 Å. (c) The evolution of the output voltage with strain.

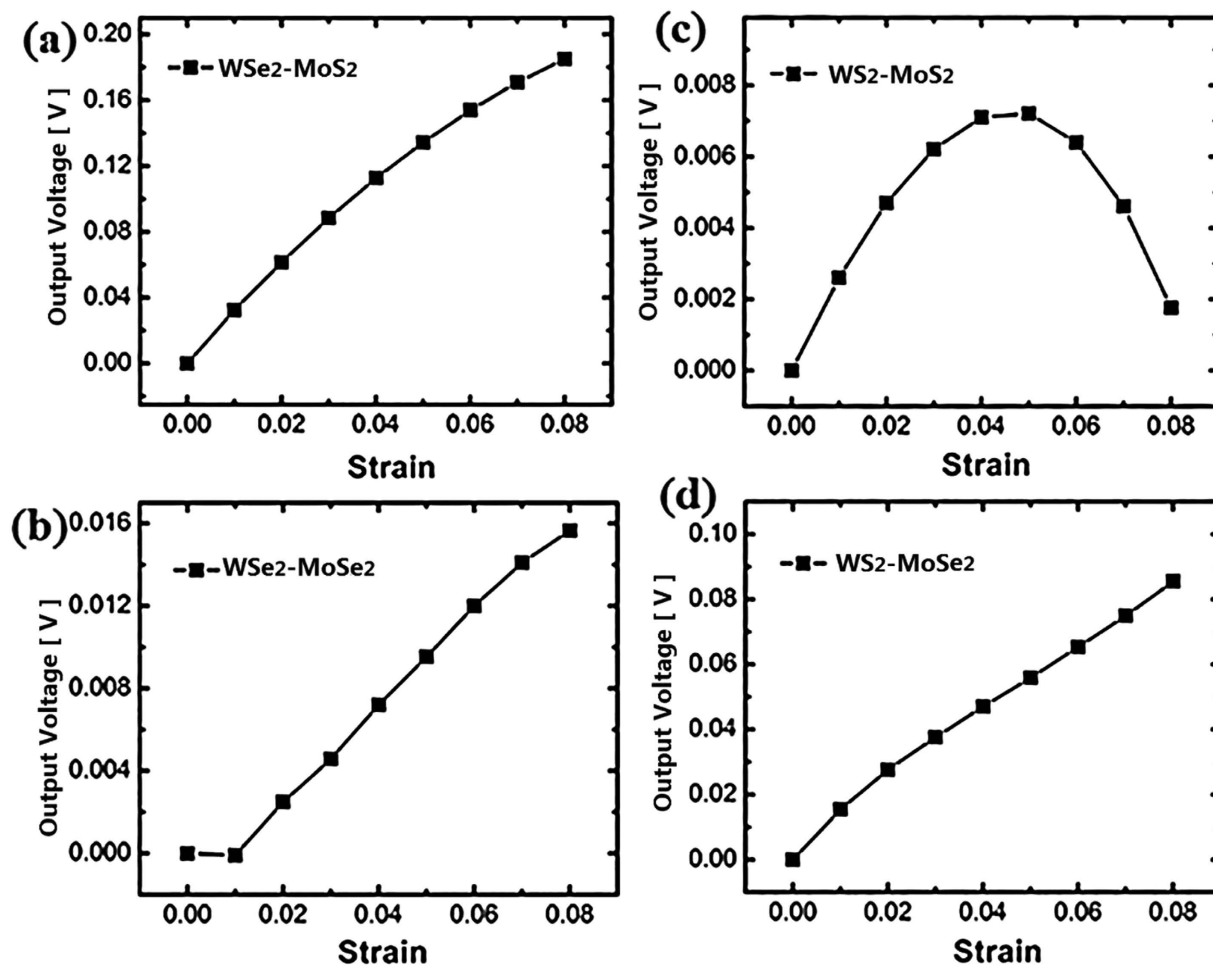


**Figure 9.** The output voltage as a function of strain for 4 heterojunction structures: (a)  $\text{WSe}_2\text{-MoS}_2$  (b)  $\text{WSe}_2\text{-MoSe}_2$  (c)  $\text{WS}_2\text{-MoS}_2$  (d)  $\text{WS}_2\text{-MoSe}_2$

Strain = 8%	Output [ V ]	EPD [ eV ]
$\text{MoS}_2$ PN junction	0.310	1.174
$\text{WSe}_2$ PN junction	0.328	1.089
$\text{MoSe}_2$ PN junction	0.189	0.992
$\text{WS}_2$ PN junction	0.356	1.369
$\text{WSe}_2\text{-MoS}_2$ heterojunction	0.185	2.543
$\text{WS}_2\text{-MoS}_2$ heterojunction	0.00721	0.296
$\text{WS}_2\text{-MoSe}_2$ heterojunction	0.0855	2.377
$\text{WSe}_2\text{-MoSe}_2$ heterojunction	0.0157	0.215

**Table 1.** The comparison of output voltage and EPD for different structures.

for even number of layers<sup>26</sup>. Our study shows that the structures with even number of layers still have strong output, indicating a distinct underlying physical principle with the device by undoped nanosheet. It should be noted that as the larger size (Larger width, length and layer number), the output voltage of our device tends to converge to a constant value. Our study suggests a mechano-electric generator with weak dependence on dimension and size, which is exceedingly favourable for industrial application.

### Doping effect

Precisely control the dopant position and number is the main challenge for the application of low-dimensional nanomaterials. This inaccuracy in fabrication induces variations in mechanic and



electronic properties of 2D materials and devices<sup>48,49</sup>. Therefore we investigate the variation of output voltage upon the various doping positions in MoS<sub>2</sub> nanoribbon mechano-electric converter. As displayed by Fig. 7(a), the various combinational doping positions of P and Cl are denoted by P(m, n), where m, n are the atomic ordinal number of doping atoms P and Cl. P replaces S at left side while Cl is doping at right side. The variation of output voltage upon the doping combinations is exhibited in Fig. 7(b). The combination P(4,4) has the nearest distance between P and Cl while they reaches farthest away from each other in P(1,1). Generally the output voltage randomly fluctuates within small range from 0.301 V to 0.312 V. This limited variation modulated by various doping positions is favourable for future industrial applications. The doping concentration effect are also revealed in our study. 2 pairs of doping atoms are introduced in our device, as shown in Fig. 7(c). The dependence of output voltage on strain is demonstrated in Fig. 7(d). It increases linearly as larger strain. However, the output is lowered by higher doping concentration compared to that of the device based on one pair of doping atoms. The output is 0.028 V and 0.256 V for the device applied by 1% and 8% strain, respectively.

### TMDCs heterojunction based device

We also investigate the mechano-electric converter based on TMDCs heterojunctions. Fig. 8(a). displayed the WSe<sub>2</sub>-MoS<sub>2</sub> heterojunction based mechano-electric generator. The left part is WSe<sub>2</sub> nanoribbon and the right counterpart is MoS<sub>2</sub> nanoribbon. Fig. 8(b) reveals the electrostatic potential distribution along transport direction in the central region for the device under 0%, 4% and 8% tensile strain, respectively. The EPD mainly occurs at the narrow connection region between WSe<sub>2</sub> and MoS<sub>2</sub> nanoribbon. This radical change in electrostatic potential arises from the great difference between the work functions of WSe<sub>2</sub> and MoS<sub>2</sub> monolayer. As opposite to the regulatory change of EPD by strain in MoS<sub>2</sub> PN junction, increasing strain causes larger EPD in heterojunctions. Fig. 8(c) reveals the output performance as a function of strain. The output voltage increases with larger strain and 0.185 V can be achieved by 8% strain. Our observation suggests that MoS<sub>2</sub> PN junction based device has better output performance than TMDCs based heterojunctions.

Fig. 9 shows the output voltage as a function of strain for 4 different heterojunctions: a) WSe<sub>2</sub>-MoS<sub>2</sub> (b) WSe<sub>2</sub>-MoSe<sub>2</sub> (c) WS<sub>2</sub>-MoS<sub>2</sub> (d) WS<sub>2</sub>-MoSe<sub>2</sub>. As shown in Fig. 9(c), WS<sub>2</sub>-MoS<sub>2</sub> heterojunction reaches maximum output of  $7.21 \times 10^{-3}$  V under 5% strain, then reduces significantly by larger strain. For the other 3 structures, the output voltage is generally increasing by larger strain. Among these structures, WSe<sub>2</sub>-MoS<sub>2</sub> heterojunction achieves the largest output of 0.185 V under 8% strain. However, this is still inferior to the performance of MoS<sub>2</sub> PN junction, which possesses the output of 0.310 V under the equal strain. WSe<sub>2</sub>-MoS<sub>2</sub> and WS<sub>2</sub>-MoSe<sub>2</sub> can obtain the output voltage with a value of one order of magnitude larger than those of the other two structures, indicating that the enhanced output can be achieved by the TMDCs heterojunction based on different chalcogen materials. Table 1 summarizes the output voltage and EPD for 8 different TMDCs PN junctions and heterojunctions, all of which are in the same size of  $5 \times 9$  ( $N_a = 5$ ,  $N_b = 9$ ). The heterojunction structures with higher EPD can achieve higher output voltage. Larger EPD is attributed to larger difference in work functions of distinct nanoribbons at opposite sides. This rule is also applied appropriately to the TMDCs PN junctions, among which the output voltage and EPD both reach largest value in WS<sub>2</sub> PN junction.

### Summary

In summary, enlightened by the intrinsic piezoelectricity of TMDCs based two dimensional monolayer, we have designed and simulated a novel piezoelectric device realized by MoS<sub>2</sub> monolayer based PN junction. Its electromechanical property was simulated by first-principle calculations. 0.31 V of output voltage can be achieved by  $0.051 \text{ eV}/\text{\AA}^3$  of the laterally tensile stress, which leads to 8% strain in transport direction. We have also demonstrated the time domain-output voltage in the case of the applied stress in Sine waveform. The investigation on size-dependent performance demonstrates that by increasing width, length and layer number the output will finally converge to constant output. Our investigation on the doping effect shows that various doping positions affect slightly on the output voltage and the low concentration gives rise to higher output performance. The piezoelectric performance based on 4 different TMDCs-heterojunction were also simulated. We conclude that the structure with higher EPD can obtain higher output voltage. Our study suggests a novel TMDCs PN junction and heterojunction based mechano-electric generator with high output voltage. This may open up a suite of applications in 2D-TMDCs based piezoelectric transistor.

### References

1. Tian, B. *et al.* Coaxial silicon nanowires as solar cells and nanoelectronic power sources. *Nature* **449**, 885–889 (2007).
2. Elliott, A. D. T. & Mitcheson, P. D. Implementation of a Single Supply Pre-biasing Circuit for Piezoelectric Energy Harvesters. *Procedia Eng.* **47**, 1311–1314 (2012).
3. Dahiya, R. S., Adami, A., Valle, M., Lorenzelli, L. & Metta, G. CMOS Implementation of POSFET Tactile Sensing Arrays with on Chip Readout. in *2010 Fourth International Conference on Sensor Technologies and Applications (SENSORCOMM)* 80–83 (2010).
4. Donelan, J. M. *et al.* Biomechanical Energy Harvesting: Generating Electricity During Walking with Minimal User Effort. *Science* **319**, 807–810 (2008).
5. Chen, L., Xu, X., Zeng, P. & Ma, J. Integration of Energy Harvester for Self-Powered Wireless Sensor Network Nodes. *Int. J. Distrib. Sens. Netw.* **2014**, e782710 (2014).

6. Adami, A., Dahiya, R. S., Collini, C., Cattin, D. & Lorenzelli, L. POSFET touch sensor with CMOS integrated signal conditioning electronics. *Sens. Actuators Phys.* **188**, 75–81 (2012).
7. Anton, S. R. & Sodano, H. A. A review of power harvesting using piezoelectric materials (2003–2006). *Smart Mater. Struct.* **16**, R1 (2007).
8. Blick, R. H. & Grifoni, M. FOCUS ON NANO-ELECTROMECHANICAL SYSTEMS. *New J. Phys.* **7**, null (2005).
9. Lakshmanan, S. B. *et al.* Local Field Enhanced Au/CuS Nanocomposites as Efficient Photothermal Transducer Agents for Cancer Treatment. *J. Biomed. Nanotechnol.* **8**, 883–890 (2012).
10. Shin, S.-H., Lee, M. H., Jung, J.-Y., Seol, J. H. & Nah, J. Piezoelectric performance enhancement of ZnO flexible nanogenerator by a CuO–ZnO p–n junction formation. *J. Mater. Chem. C* **1**, 8103–8107 (2013).
11. Shin, S.-H. *et al.* Lithium-Doped Zinc Oxide Nanowires–Polymer Composite for High Performance Flexible Piezoelectric Nanogenerator. *ACS Nano* **8**, 10844–10850 (2014).
12. Shin, S.-H., Kim, Y.-H., Jung, J.-Y., Lee, M. H. & Nah, J. Solvent-assisted optimal BaTiO<sub>3</sub> nanoparticles-polymer composite cluster formation for high performance piezoelectric nanogenerators. *Nanotechnology* **25**, 485401 (2014).
13. Wang, Z. L. & Song, J. Piezoelectric Nanogenerators Based on Zinc Oxide Nanowire Arrays. *Science* **312**, 242–246 (2006).
14. Lu, M.-P. *et al.* Piezoelectric Nanogenerator Using p-Type ZnO Nanowire Arrays. *Nano Lett.* **9**, 1223–1227 (2009).
15. Gao, Y. & Wang, Z. L. Equilibrium potential of free charge carriers in a bent piezoelectric semiconductive nanowire. *Nano Lett.* **9**, 1103–1110 (2009).
16. Chandratte, S. & Sharma, P. Coaxing graphene to be piezoelectric. *Appl. Phys. Lett.* **100**, 023114 (2012).
17. Yilei Li, Y. R. Probing symmetry properties of few-layer MoS<sub>2</sub> and h-BN by optical second-harmonic generation. *Nano Lett.* **13**, 3329–3333 (2013).
18. Mak, K. F., Lee, C., Hone, J., Shan, J. & Heinz, T. F. Atomically Thin MoS<sub>2</sub>: A New Direct-Gap Semiconductor. *Phys. Rev. Lett.* **105**, 136805 (2010).
19. Duerloo, K.-A. N., Ong, M. T. & Reed, E. J. Intrinsic Piezoelectricity in Two-Dimensional Materials. *J. Phys. Chem. Lett.* **3**, 2871–2876 (2012).
20. Bertolazzi, S., Brivio, J. & Kis, A. Stretching and Breaking of Ultrathin MoS<sub>2</sub>. *ACS Nano* **5**, 9703–9709 (2011).
21. Coleman, J. N. *et al.* Two-Dimensional Nanosheets Produced by Liquid Exfoliation of Layered Materials. *Science* **331**, 568–571 (2011).
22. K. H. Michel, B. V. Phonon dispersions and piezoelectricity in bulk and multilayers of hexagonal boron nitride. *Phys. Rev. B* **83**, (2011).
23. Cao, T. *et al.* Valley-selective circular dichroism of monolayer molybdenum disulphide. *Nat. Commun.* **3**, 887 (2012).
24. Mak, K. F., He, K., Shan, J. & Heinz, T. F. Control of valley polarization in monolayer MoS<sub>2</sub> by optical helicity. *Nat. Nanotechnol.* **7**, 494–498 (2012).
25. Zhu, H. *et al.* Observation of piezoelectricity in free-standing monolayer MoS<sub>2</sub>. *Nat. Nanotechnol.* **10**, 151–155 (2015).
26. Wu, W. *et al.* Piezoelectricity of single-atomic-layer MoS<sub>2</sub> for energy conversion and piezotronics. *Nature* **514**, 470–474 (2014).
27. Jiang, T. *et al.* Valley and band structure engineering of folded MoS<sub>2</sub> bilayers. *Nat. Nanotechnol.* **9**, 825–829 (2014).
28. Brandbyge, M., Mozos, J.-L., Ordejón, P., Taylor, J. & Stokbro, K. Density-functional method for nonequilibrium electron transport. *Phys. Rev. B* **65**, 165401 (2002).
29. Kohn, W. & Sham, L. J. Self-Consistent Equations Including Exchange and Correlation Effects. *Phys. Rev.* **140**, A1133–A1138 (1965).
30. Monkhorst, H. J. & Pack, J. D. Special points for Brillouin-zone integrations. *Phys. Rev. B* **13**, 5188–5192 (1976).
31. Perdew, J. P., Burke, K. & Ernzerhof, M. Generalized Gradient Approximation Made Simple. *Phys. Rev. Lett.* **77**, 3865–3868 (1996).
32. Grimme, S. Semiempirical hybrid density functional with perturbative second-order correlation. *J. Chem. Phys.* **124**, 034108 (2006).
33. Li, Y., Zhou, Z., Zhang, S. & Chen, Z. MoS<sub>2</sub> Nanoribbons: High Stability and Unusual Electronic and Magnetic Properties. *J. Am. Chem. Soc.* **130**, 16739–16744 (2008).
34. Yue, Q. *et al.* Bandgap tuning in armchair MoS<sub>2</sub> nanoribbon. *J. Phys. Condens. Matter* **24**, 335501 (2012).
35. Song, J., Zhou, J. & Wang, Z. L. Piezoelectric and semiconducting coupled power generating process of a single ZnO belt/wire. A technology for harvesting electricity from the environment. *Nano Lett.* **6**, 1656–1662 (2006).
36. Sun, Q.-Q. *et al.* The physics and backward diode behavior of heavily doped single layer MoS<sub>2</sub> based p-n junctions. *Appl. Phys. Lett.* **102**, 093104 (2013).
37. J. F. Nye. *Physical Properties of Crystals: Their Representation by Tensors and Matrices*, Ch. 7, 130 (Clarendon, 1985).
38. Ong, M. T. & Reed, E. J. Engineered Piezoelectricity in Graphene. *ACS Nano* **6**, 1387–1394 (2012).
39. Wilson, J. A. & Yoffe, A. D. The transition metal dichalcogenides discussion and interpretation of the observed optical, electrical and structural properties. *Adv. Phys.* **18**, 193–335 (1969).
40. Li, H., Wu, J., Yin, Z. & Zhang, H. Preparation and Applications of Mechanically Exfoliated Single-Layer and Multilayer MoS<sub>2</sub> and WSe<sub>2</sub> Nanosheets. *Acc. Chem. Res.* **47**, 1067–1075 (2014).
41. Sutar, S. *et al.* Reconfigurable p-n Junction Diodes and the Photovoltaic Effect in Exfoliated MoS<sub>2</sub> Films. *Appl. Phys. Lett.* **104**, 122104 (2014).
42. Wu, J. *et al.* Layer thinning and etching of mechanically exfoliated MoS<sub>2</sub> nanosheets by thermal annealing in air. *Small Weinb. Bergstr. Ger.* **9**, 3314–3319 (2013).
43. Lee, J.-U., Park, J., Son, Y.-W. & Cheong, H. Anomalous excitonic resonance Raman effects in few-layered MoS<sub>2</sub>. *Nanoscale* **7**, 3229–3236 (2015).
44. Salmani-Jelodar, M., Tan, Y. & Klimeck, G. Single layer MoS<sub>2</sub> band structure and transport. in *Semiconductor Device Research Symposium (ISDRS)*, 2011 International 1–2 (2011).
45. Caro, M. A., Schulz, S. & O'Reilly, E. P. Comparison of stress and total energy methods for calculation of elastic properties of semiconductors. *J. Phys. Condens. Matter* **25**, 025803 (2013).
46. Yue, Q. *et al.* Mechanical and electronic properties of monolayer MoS<sub>2</sub> under elastic strain. *Phys. Lett. A* **376**, 1166–1170 (2012).
47. Dahiya, R. S., Metta, G. & Valle, M. Piezoelectric polymer oxide semiconductor field effect transistor (POSFET) devices for touch sensing. in *2nd International Workshop on Electron Devices and Semiconductor Technology, 2009. IEDST*, **09**, 1–5 (2009).
48. Yu, S., Xiong, H. D., Eshun, K., Yuan, H. & Li, Q. Phase transition, effective mass and carrier mobility of MoS<sub>2</sub> monolayer under tensile strain. *Appl. Surf. Sci.* **325**, 27–32 (2015).
49. Eshun, K., Xiong, H. D., Yu, S. & Li, Q. Doping induces large variation in the electrical properties of MoS<sub>2</sub> monolayers. *Solid-State Electron.* **106**, 44–49 (2015).

## Acknowledgements

This work was supported in part by the U.S. NSF Grant ECCS-1407807 and in part by Virginia Microelectronics Consortium research grant.

### Author Contributions

Q.L. designed the project and study. Q.L. and S.Y. designed the device structures. S.Y. performed the simulation and computation. Q.L., K.E. and H.Z. analyzed the simulation methods, processes and data. S.Y. wrote the draft of manuscript. Q.L. prepared Fig. 1 and S.Y. prepared Figs 2–9 and Table 1. Q.L. and K.E. revised the paper. H.Z. reviewed the manuscript and figures.

### Additional Information

**Competing financial interests:** The authors declare no competing financial interests.

**How to cite this article:** Yu, S. *et al.* Novel Two-Dimensional Mechano-Electric Generators and Sensors Based on Transition Metal Dichalcogenides. *Sci. Rep.* **5**, 12854; doi: 10.1038/srep12854 (2015).



This work is licensed under a Creative Commons Attribution 4.0 International License. The images or other third party material in this article are included in the article's Creative Commons license, unless indicated otherwise in the credit line; if the material is not included under the Creative Commons license, users will need to obtain permission from the license holder to reproduce the material. To view a copy of this license, visit <http://creativecommons.org/licenses/by/4.0/>